Numerical Analysis of Ion Temperature Gradient Driven Drift Wave

Ando, Youji
Interdisciplinary Graduate School of Engineering Sciences, Kyushu University

Ito, Sanae-I.
Research Institute for Applied Mechanics, Kyushu University

Yagi, Masatoshi
Research Institute for Applied Mechanics, Kyushu University

https://doi.org/10.15017/26795

出版情報：九州大学応用力学研究所所報. 129, pp.47-59, 2005-09. Research Institute for Applied Mechanics, Kyushu University

Numerical Analysis of Ion Temperature Gradient Driven Drift Wave

Youji ANDOU *1, Sanae -I. ITOH *2, Masatoshi YAGI*2,
E-mail of corresponding author: *youjiji@riam.kyushu-u.ac.jp*

(Received July 29, 2005)

Abstract

We have develpoed global ITG (Ion Temperature Gradient Driven Drift Wave) turbulence code to investigate anomalous ion transport in tokamak plasmas. The gyro-fluid model is extended to incorporate accurate form of neoclassical viscosity. Firstly, we have performed the linear analysis of ITG mode using this code. The dependence of growth rate on various parameters are examined. Next, we have done nonlinear simulations to investigate neoclassical effect on zonal flow damping and saturation amplitude of ITG turbulnce. The weak depdenence of saturation level on neoclassical viscosity is found in our simulations.

Key words : *ITG mode, ITG turbulence, anomalous transport*

1. Introduction

To achieve thermonuclear condition in a tokamak, it is necessary to confine the plasma for a sufficient time. Confinement is limitted by thermal conduction and convection process but radiation is also a source of energy loss.

In the absence of instabilities, the confinement of tokamak plasma is determined by Coulomb collisions, so called neoclassical transport theory. Unfortunately, the transport which occurs in reality does not agree with the values predicited by neoclassical theory. Especially, the thermal transport by electrons can be up to two orders of magnitude higher than predicted one.

It is thought that the observed anomalous transport is due to microinstability of plasma, which causes the particles and the energy to escape at a higher rate[1]. Microinstabilites provide a mechanism for the generation of fine scale plasma turbulence and therefore is importrant for an understanding of anomalous transport in tokamaks.

Recently, a subclass of gradient-driven turbulence, the ion-temperature-gradient (ITG) driven turbulence has recieved considerable attension by theoreticians[2, 3]. This is partly due to the fact that in large neutral beam heated tokamaks, the main thermal losses occur on the ion channel, therefore, ITG turbulence may play important role in confinement. The transport database studies in the framework of the international thermonuclear experimental reactor(ITER) have demonstrated that a machine of the ITER type would perform better if the present data can extrapolated according to the so called gyro-Bohm scaling. Several numerical studies are performed focusing on the ρ_* scaling of ion thermal transport where ρ_* is the ratio of the ion Larmor radius to a plasma minor radius. Early results from global gyro-kinetic codes pointed to a Bohm scaling for the ion thermal conductivity, however, the latest simulations which include the self-consistent poloidal flows address the gyro-Bohm scaling if the system size increases[4]. The similar study is also performed based on gyro-fluid model which also supports the gyro-Bohm scaling[5].

These studies show that the zonal flow plays an important role for the saturation of ITG turbulence. Therefore, the realistic model for neoclassical viscosity should be incorporated in the model, which contributes to the damping of the zonal flow. In this thesis, we extended the gyro-fluid model proposed by Ottaviani et. al[5] which includes the ion parallel flow and ion neoclassical viscosity. We analyze ITG mode and ITG turbulence by using the gyro-fluid model. The linear growth rate of ITG mode is investigated by some parameters, for example, toroidal mode number, shear parameter etc. The nonlinear effects of ITG turbulence are investigated for ITG turbulence saturation and ion heat diffusion coefficient, χ.

This thesis is organized as follows. In Chapter 2, ITG turbulence in tokamak plasma is reviewed. Theoretical approach of ITG turbulence is discussed and

*1 Interdisciplinary Graduate School of Engineering Sciences, Kyushu University
*2 Research Institute for Applied Mechanics, Kyushu University

results by numerical simulations are shown. In Chapter 3, we extend the gyro-fluid model to incorporate accurate form of neoclassical viscosity. The linear analysis of ITG mode is performed using this model. The dependence of growth rate on various parameters are investigated. Next, nonlinear simulations are performed and neoclassical effect on zonal flow damping and saturation amplitude of ITG turbulence are investigated. Finally, in Chapter 4, summary and discussions are given.

2. Reviews

The anomalous transport is considered to be induced by micro-turbulence. The temperature gradient driven instabilities are proposed as the plausible candidates responsible for anomalous ion thermal transport. To understand the physical mechanism of anomalous transport and to reduce it, are quite important to attain the self-ignition condition. In this chapter, theorectical approach on anomalous transport related with ITG turbulence and the $\mathbf{E}\times\mathbf{B}$ shear suppression on the turbulence are reviewed[6, 7, 8, 9, 10, 11, 12, 13, 14, 15, 16].

2.1 ITG Mode Instability

The unstable drift wave is analyzed using the drift-kinetic equation[17]:

$$\frac{\partial f_i}{\partial t}+\frac{\mathbf{E}\times\mathbf{B}}{B^2}\cdot\nabla f_i+v_z\frac{\partial f_i}{\partial z}+\frac{e}{M}E_z\frac{\partial f_i}{\partial v_z}=0. \quad (1)$$

where f_i is the ion distribution function and the z-axis is taken to be parallel to the magnetic field $\mathbf{B}$. The use of the drift-kinetic equation implies that we neglect the ion polarization drift as well as corrections of order $k_\perp^2\rho_i^2$ to the ion $\mathbf{E}\times\mathbf{B}$ drift. We assume the equilibrium distribution function for ion is Maxwellian given by

$$f_0(x,v)=n_0(x)\left(\frac{M}{2\pi T_0(x)}\right)^{3/2}exp\left(-\frac{Mv^2}{2T_0(x)}\right). \quad (2)$$

Here the electrostatic perturbation $\mathbf{E}=-\nabla\phi$ is considered. Linearizing the drift-kinetic euqation and integrating the velocity space, ion density perturbation n_{i1} is obtained as

$$n_{i1}=-\frac{n_{i0}e\phi}{T_{i0}}+\frac{e\phi}{T_{i0}}\int_{-\infty}^{\infty}\frac{F_{i0}(v_z)dv_z}{\omega-k_zv_z}\times\left\{\omega-k_yv_{di}\left[1-\eta_i\left(\frac{1}{2}-\frac{v_z^2}{2v_{t,i}^2}\right),\right]\right\} \quad (3)$$

where an ion diamagnetic drift is given by

$$v_{di}=\frac{T_{i0}}{n_{i0}eB_{z0}}\frac{dn_{i0}}{dx}, \quad (4)$$

and a dimensionless measure of the ion temperature gradient is

$$\eta_i=\frac{dlnT_{i0}/dx}{dlnn_{i0}/dx}. \quad (5)$$

(ω,k) is the real frequency and the wave number of the mode, respectively. The one-dimensional Maxwellian distribution is also introduced;

$$F_{i0}(v_z)=n_{i0}\left(\frac{M}{2\pi T_{i0}}\right)^{1/2}exp\left(-\frac{Mv_z^2}{2T_{i0}}\right). \quad (6)$$

For electrons, we assume the adiabatic response:

$$n_{e1}=\frac{n_{e0}e\phi}{T_{e0}}. \quad (7)$$

By setting $n_{e1}=n_{i1}$, the dispersion relation is obtained by

$$1+\frac{T_{i0}}{T_{e0}}=D(\omega), \quad (8)$$

where

$$D(\omega)=\frac{1}{n_{i0}}\int_{-\infty}^{\infty}\frac{F_{i0}(v_z)dv_z}{\omega-k_zv_z}\times\left\{\omega-k_yv_{di}\left[1-\frac{\eta_i}{2}\left(1-\frac{v_z^2}{v_{t,i}^2}\right)\right]\right\}. \quad (9)$$

Using the Nyquist diagram technique, it is found that the unstable drift wave exsists for

$$\eta_i>2+\frac{4}{\Lambda}\frac{T_{i0}}{T_{e0}}\left(1+\frac{T_{i0}}{T_{e0}}\right), \quad (10)$$

where

$$\Lambda=\frac{\eta_ik_y^2v_{di}^2}{k_z^2v_{t,i}^2}. \quad (11)$$

In the limit of $\Lambda\gg 1$, the condition for instability will approach a limiting case

$$\eta_i>2. \quad (12)$$

However, since the diamagnetic drift speed is generally much less than the ion thermal speed, the ratio k_z/k_y must be exceedingly small to give $\Lambda\gg 1$. In the cases where arbitrarilty small k_z values are not allowed, such as in a torus geometry and the existence of magnetic shear, the stability is improved. On the other hand, inclusion of shorter wavelength modes is found to lower the instability threshold for η_i to values close to unity.

Over the years, many authors have attemped to expain experimental results on anomalous transport in tokamak using theoretical models of drift wave turulence. By use of realistic geometries and advanced computational techniques, the agreement between experimental data and the simulation results appears to be improved remarkably.

2.2 Bohm Scaling and Gyro-Bohm Scaling

2.2.1 Scale Invariance

If the turbulence is on a microscopic scale, for example on the scale-length of the ion Larmor radius ρ_s measured at the electron temperature, the collisionless skin depth c/ω_{pe} with c light speed and ω_{pe} the electron plasma frequency, or resistive layer width $a/\sqrt{\tau_R/\tau_A}$

with τ_R the resistive diffusion time and τ_A the Alfven time, then the scale invariance technique can be applied to the equation for the flucutations. This processure leads to scalings for the fluctuations and the corresponding turbulent transport. For example, the potential fluctuation takes the form[19)]

$$\frac{e\phi}{T} = \frac{\rho_s}{L_n} f(\nu_*, \beta, \cdots), \tag{13}$$

and the diffusion coeffcient

$$D = D_{gB} f(\nu_*, \beta, \cdots), \tag{14}$$

where the gyro-Bohm coefficient is

$$D_{gB} = \frac{\rho_s}{L_n} D_B, \tag{15}$$

with $D_B = T/eB$ the Bohm coefficient and $L_n = n/\frac{dn}{dx}$ the density scale length. And f is the function of non-dimensional parameters such as the collision frequency ν^* and the plasma beta value β. On the other hand, if the flucuations have a scale l which is proportional to a, rather than ρ_s, but still satisfies $l \ll a$, then

$$\frac{e\phi}{T} \sim \frac{l}{a}, \tag{16}$$

and

$$D = D_B f(\nu_*, \beta, \cdots). \tag{17}$$

The calculation of specific forms for the function f requires a model for the nonlinear saturation. A simple bound is given by the so-called mixing-length estimate, in which it is assumed that the instability drive is removed when the perturbations reach an amplitude such that the perturbed gradients equal the equilibrium gradient. Thus for drift waves driven by the density gradient this estimate gives the density fluctuation n_{k1} of

$$k_\perp n_{k1} \sim \frac{n_{k0}}{L_n}, \tag{18}$$

and since the density perturbations satisfy the Boltzmann relation, the saturated potential flucutation is

$$\frac{e\phi}{T} \sim \frac{1}{k_\perp L_n}. \tag{19}$$

The quasi-linear formula for electrostatic fluctuations is given by

$$\Gamma = \left\langle \int \sum_k Im\left(\frac{1}{\omega - k_\parallel v_\parallel}\right) \frac{k_y^2}{B^2} |\phi|^2 \frac{df}{dr} d^3v \right\rangle. \tag{20}$$

Inserting eq.(2.19) into eq.(2.20) gives

$$D \sim \frac{\gamma}{k_\perp^2}, \tag{21}$$

where γ is the imaginary part of ω, which is the growth rate of the mode. This result can also be interpreted as a balance between the linear growth of a mode and a stabilization from turbulent diffusion $k_\perp^2 D$.

2.2.2 Verification of Scaling Law by Numerical Simulations

Based on gyro-kinetic simulation[4)], it is found that the correlation functions for density perturbations are found to be self-similar for different tokamak size as is shown in figure 1. The correlation function decays exponentially and no significant tails at radial separations exist. It is also shown that fluctuation scale length is microscopic and independent of device size. The probability distribution function for the radial extent of test particles decays exponentially with no significant tails at large amplitudes, which implies the transport is diffusive.

We might expect the transport scaling is gyro-Bohm because the fluctuation is microscopoic and test particle is diffusive. Figure 2 shows the ion heat conductivity vs tokamak minor radius. It is seen that local ion heat conductivity exhibits Bohm-like scaling corresponding to recent tokamak experiments($a < 400\rho_i$) even if turbulence eddy is independent of device size. As the device size further is increased up to $a = 1000\rho_i$, there is a gradual transition from Bohm-like scaling to gyro-Bohm scaling. Recent transport studies of the JET tokamak and a scan of power thresholds for the formation of internal transport barriers show a similar trend.

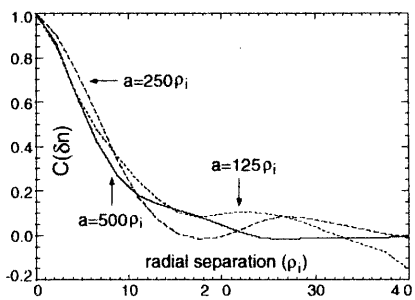

Fig. 1 Radial correlation function for density perturbation cited from Ref.[4)].

2.3 Zonal Flow Formation and Turbulence Suppression

Zonal flow and turbulence interact each other. Zonal flow is driven by turbulence and is known to strongly influence the level of turbulence and transport. Zonal flows are generated by the Reynolds stress and can be considered as a nonlinear modulational instability associated with the inverse cascade of the turbulence energy. The plasma density and temperature fluctuations can generate mean poloidal flow(zonal flow), which is driven by the divergence of the wave energy density flux or, equivalently, the gradient of the Reynolds stress. The

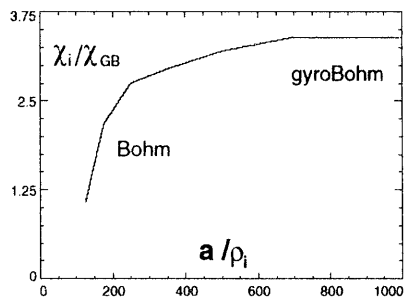

Fig. 2 Ion heat conductivity vs tokamak minor radius cited from Ref.[4].

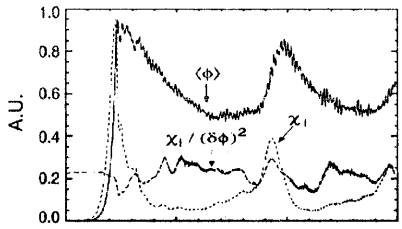

Fig. 3 The time history for zonal flow amplitude$<\phi>$, ion heat conductivity χ_i, turbulence intensity $(\delta\phi)^2$ cited from Ref.[21].

properties of the turbulence required for flow acceleration are that the fluctuations be radially propagating waves, and there be a radial asymmetry across the fluctuation spectrum. The kinetic energy of the generated flow is extracted from expansion free energy stored in via the fluctuations. As zonal flow speed and shear increase, collisional and turbulent viscosity and shear-enhanced decorrelation of fluctuations can be expected to self-consistently limit mean flow evolution. From figure 3, we find turbulence transport level is strongly influenced by zonal flow. The ITG evolves from a linear phase of exponential growth to a nonlinear stage in which zonal flows are generated. When effective shearing rate, or root mean square shearing rate increases, the ITG turbulence and transport are significantly reduced. Zonal flow is slowly damped by the ion-ion collisions and becomes weaker. When the effective shearing rate is below the growth rate, the ITG turbulence grows again and drives zonal flow. These turbulence-zonal-flow interactions, modulated by collisions, result in a cyclic, bursting behavior of fluctuations, transport, and zonal flow. In the next section, the poloidal flow damping for collision and collisionless process is discussed.

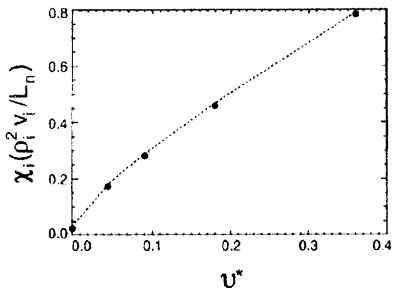

Fig. 4 Ion heat conductivity vs ion-ion collision frequency cited from Ref.[21].

2.4 Neoclassical Flow Damping

Recent advances in gyrofluid simulation of ion temperature gradient mode in tokamaks have shown that the predominant saturation mechanism for the instability is the production of axisymmetric, primarily poloidal flows which vary with radius and serve to shear stabilize to the instability. The damping of such poloidal flows is, thus, critically important in determing the turbulence level to be expected.

First, collisionless process of poloidal flow damping is explained. From gyro-kinetic equation, the poloidal flow equation is derived by [22]

$$u_p = (1 + 1.6q^2/\epsilon^{1/2})^{-1} u_p(0), \tag{22}$$

where u_p is the poloidal flow velocity, q is the safety factor and ϵ is inverse aspect ratio. It is shown that the poloidal flow is not damped by collisionless process. At least near the marginal stability, where the nonlinear damping of poloidal flows should be negligible, and in the sufficiently collisionless regimes of interest (deep in the banana regime), the level of poloidal rotation should be larger, and the ITG turbulence level and transport should be considerably smaller than predictions made by gyrofluid simulations which entail linear collisionless damping. With respect to the collisional process of poloidal flow damping, it is shown that the poloidal flow is damped by collisional process[23, 24]. Figure 4 shows the dependence of diffusion coefficient on ion-ion collision frequency. As the collision frequency increases, the diffusion coefficient becomes larger, so that the zonal flow becomes weaker, the turbulence transport is enhanced and the plasma confinement becomes worse. It is conducted that the collisional poloidal flow is quit different from the collisionless poloidal flow.

3. Numerical Analysis

In this chapter, we drive the fluid moment equations for ITG mode and analyze the dependence of the growth

rate on key parameters such as toroidal mode number, the magnetic shear, η_i parameter etc. Next, nonlinear simulation of ITG turbulence is performed and results are analyzed.

3.1 Model Equations

We consider a high temperature plasma of major radius R and minor radius a with a toroidal magnetic field B_0 in the toroidal coordinate (r, θ, ϕ). The global gyro-fluid model was proposed to investigate the ITG turbulence and transport scaling[5]. In order to study the relation between the zonal flow damping and the ITG saturation, we incorporate the neoclassical viscosity relevant in the Banana-Plateau regime into the model. This model consists of the ion continuity equation:

$$\frac{dW}{dt} + \kappa_n \frac{1}{r}\frac{\partial \phi}{\partial \theta} + A\nabla_{\|} v_{i\|} + A v_{i\|}\nabla_{\|} n_i = \epsilon_a \hat{\omega}_d F + \rho_* \frac{q}{\epsilon}\mu_i^{neo}\frac{\partial U_{pi}}{\partial r} - \rho_*^2 \mu \nabla_{\perp}^4 F, \quad (23)$$

parallel momentum equation:

$$\frac{dv_{i\|}}{dt} = -A\nabla_{\|}\left(\phi + \frac{p_i}{\tau}\right) + 4\mu\nabla_{\perp}^2 v_{i\|} - \mu_i^{neo} U_{pi}, \quad (24)$$

and ion temperature equation:

$$\frac{3}{2}\left(\frac{dT_i}{dt} + \kappa_T \frac{1}{r}\frac{\partial \phi}{\partial \theta} + A v_{i\|}\nabla_{\|} T_i\right) - \left(\frac{dn_i}{dt} + \kappa_n \frac{1}{r}\frac{\partial \phi}{\partial \theta} + A v_{i\|}\nabla_{\|} n_i\right) = -\frac{2}{\sqrt{\pi}}\hat{v}_{thi} A|\nabla_{\|}|T_i + \chi_{\perp}\nabla_{\perp}^2 T_i, \quad (25)$$

where

$$n_i = \phi - \langle\phi\rangle, \quad (26)$$

$$p_i = n_i + T_i = \phi - \langle\phi\rangle + T_i, \quad (27)$$

$$W = \phi - \langle\phi\rangle - \rho_*^2\nabla_{\perp}^2(\phi + \frac{1}{\tau}p_i), \quad (28)$$

$$\nabla F \equiv \frac{c}{B_0}(\nabla\phi + \frac{1}{eZ\bar{n}_i}\nabla p_i), \quad (29)$$

$$n_e = \frac{n_0 e}{T_e}\phi, \quad (30)$$

$$U_{pi} = v_{i\|} + \rho_* \frac{q}{\epsilon}\frac{\partial F}{\partial r}, \quad (31)$$

$$\mu_i^{neo} = \frac{0.66\sqrt{\epsilon}\nu_i}{(1 + 1.03\nu_{i^*}{}^{1/2} + 0.31\nu_{i^*})(1 + 0.66\nu_{i^*}\epsilon^{3/2})}, \quad (32)$$

$$A = \frac{\epsilon_a}{\rho_*}, \rho_* = \frac{\rho_i}{a},$$
$$\tau = \frac{\bar{T}_e}{\bar{T}_i}, \kappa_n = -\frac{dln\bar{n}_i}{dr},$$
$$\kappa_T = -\frac{dln\bar{T}_i}{dr}, \nu_{i^*} = \nu_i qR/(\epsilon^{3/2}v_{thi}),$$
$$\hat{v}_{thi} = \frac{v_{thi}}{c_s}, \hat{\omega}_d = 2cos\theta\frac{1}{r}\frac{\partial}{\partial\theta} + 2sin\theta\frac{\partial}{\partial r},$$

and $\langle\ \rangle$ indicates flux surface average.

Three-field consists of the fluctuating parallel velocity, $v_{\|}$, the fluctuating ion temperature, T_i and the fluctuating ion density, n_i, respectively. W represents the generalized vorticity (effectively the ion guiding center density), ϕ, the electrostatic potential, U_{pi}, the ion poloidal flow and F, the generalized potential which includes the ion diamagnetic effect. To derive these equations, we assume T_e = const and the electron responce is abiabatic. μ represents the classical ion viscosity, $\mu_i{}^{neo}$, the neoclassical viscosity and ρ_i, the ion Larmor radius. $\hat{\omega}_d$ indicates the toroidal magnetic curvature effect. ϵ_a, is the inverse aspect ratio, a, the minor radius, R the major radius, $\epsilon = r_s/R$, r_s is the location of rational surface, v_{thi}, ion thermal velocity, c_s, ion sound velocity, ν_i ion-ion collision frequency, $\bar{T}_e$, $\bar{T}_e$, $\bar{n}_i$, the averaged electron temperature, ion temperature, ion density, respectively. The effect of ion Landau damping is taken into account in eq.(25). In this model, the following normalization is used;

$$\frac{t}{t_{Bohm}} \to t, \quad \frac{r}{a} \to r, \quad \frac{n_i}{\bar{n}_i} \to n_i,$$
$$\frac{T_i}{\bar{T}_i} \to T_i, \quad \frac{v_{i\|}}{c_s} \to v_{i\|}, \quad \frac{\mu}{\rho_s c_s m_i \bar{n}_i} \to \mu,$$
$$\frac{\chi_{\perp}}{\rho_s c_s} \to \chi_{\perp}, \frac{\mu_i^{neo} a}{c_s \rho_*} \to \mu_i^{neo},$$

where t_{Bohm} is the Bohm time $t_{Bohm} = a^2/\chi_{Bohm}$, $\chi_{Bohm} = cT_e/eB$, ρ_s, the Larmor radius measured at electron temperature.

3.2 Linear Mode Analysis of ITG Mode

In this section, the linear growth rate of ITG mode is calculated.

3.3 Fourier Mode Representation

A perturbed quatiny is represented by Fourier modes by

$$f(r,\theta,\zeta) = \sum_{m-mwd}^{m+mwd} f_{m,n}(r)exp[im\theta + in\zeta + (\gamma - i\omega)t], \quad (33)$$

where m is the poloidal mode number, n, the toroidal mode number, γ, the growth rate, ω, the rotation frequency and mwd is a band width of poloidal mode. Idealy, mwd should be an infinity, however, we take a finite value in the numerical calculation. Figure 5 shows the schematic view of Fourier spectrum used in this analysis. The three-field model is numerically solved by the implicit method as the initial value problem and the largest growth rate is evaluated.

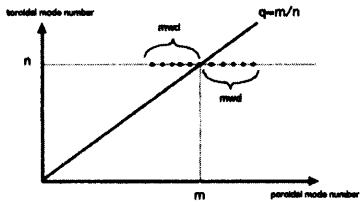

Fig. 5 Fourier spectrum for toroidal ITG mode.

3.4 Simulation Parameters

The eigenvalue and the eigenfunctions of toroidal ITG mode and slab ITG mode are calculated. We set $\hat{\omega}_d \neq 0$ for the toroidal ITG mode and $\hat{\omega}_d = 0$ for the slab ITG mode.

Initial profiles of ion density and temperature are given by

$$n_i(r) = (n_0 - n_1)\sqrt{(1-r^2)} + n_1, \tag{34}$$

$$T_i(x) = (T_0 - T_1)(1-r^2)^{prepw} + T_1, \tag{35}$$

respectively. Then, η_i parameter is evaluated as

$$\eta_i = \frac{dlnT_i/dr}{dlnn_i/dr}. \tag{36}$$

η_i parameter is controlled by changing the parameter *prepw* in ion temperature. In the linear calculation, we fix κ_n and κ_T as constant values which are evaluated on the rational surface r_s.

The model safety factor is employed;

$$q(r) = q_1(1 + (r/r_s)^a)^b + q_2, \tag{37}$$

with

$$q_2 = q_0 - q_1 \ , \ q_1 = (q_s - q_0)/(2b-1),$$
$$q_s = 2 \ or \ 3 \ , \ a = 3 \ , \ b = 1.$$

Then the shear parameter is given by

$$s = \frac{r}{q}\frac{dq}{dr} = \frac{q_1 ab(r/r_s)^a(1+(r/r_s)^a)^{b-1}}{q_1(1+(r/r_s)^a)^b + q_2}, \tag{38}$$

which is controlled by changing q_0 in q profile.

Figure 6 shows the ion density, ion temperature and q profile in the case with $prepw = 2$, $n_0 = 3[10^{20}/m^3]$, $n_1 = 0[10^{20}/m^3]$, $T_0 = 3000[eV]$, $T_1 = 0[eV]$ with $\eta_e = 4$ at $r_s = 0.6$, $q_s = 2$ and $q_s = 3$. In the following sections, we investigate the case with the same shear parameter $s = 1.8$ at $r_s = 0.6$, but different q_s value, i.e., $q_s = 2$ and $q_s = 3$.

3.5 Band Width of Poloidal Mode

Firstly, we investigate the dependence of the growth rate on the band width of poloidal mode and check the numerical convergence. Figure 7 shows the dependence of the growth rate of toroidal ITG mode on *mwd* in cases with $n = 10$, $m = 20 \pm mwd$ ($q_s = 2$) and $m = 30 \pm mwd(q_s = 3)$. It is found that the dependence of the growth rate on *mwd* is weak for $mwd > 5$ in both cases.

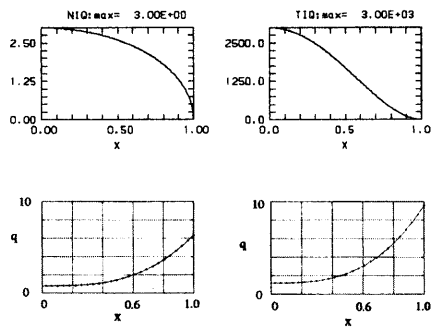

Fig. 6 Initial profiles of (a) ion density, (b) ion temperature, (c) safety factor in case with $q_s = 2$, (d) safety factor in case with $q_s = 3$.

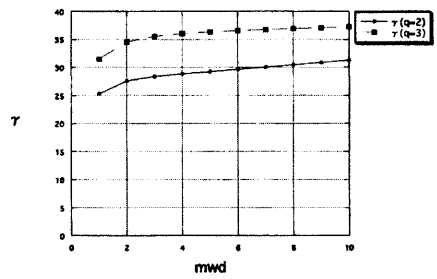

Fig. 7 The dependence of the growth rate γ on mwd which is band width is shown. The blue circle indicates $q_s = 2$ and red square $q_s = 3$.

Figure 8 shows the eigenfunction of F in cases with $mwd = 2, 6, 10$ for $q_s = 2$ or 3. It is seen that the peak of eigenfunction shifts outside according to the increase of *mwd*. This occurs due to the variation of shear parameter in the radial direction, even though κ_n and κ_T are kept constant. In the following analysis, $mwd = 5$ is used.

3.6 Eigenfunction of Toroidal/Slab ITG Mode

Figure 9 shows eigenfunctions of toroidal ITG mode $\{F, v_\parallel, T_i\}$ and n_i in the case with $q_s = 3$. The eigenfunctions are normalized by the maximum amplitude of F. It is found that F and T_i have an even parity and $v_\parallel$ has an odd parity at $r \cong 0.62$. The peak value shifts

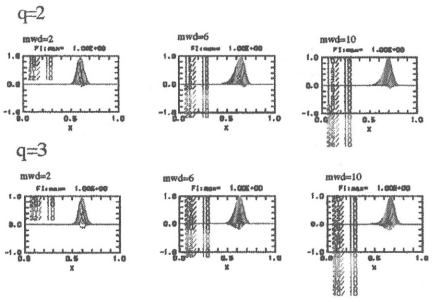

Fig. 8 Eigenfunction of F in cases with $mwd = 2, 6, 10$ for $q_s = 2$ and 3.

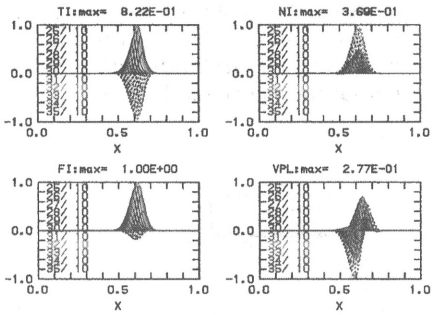

Fig. 9 Typical eigenfunctions of toroidal ITG mode in case with $q_s = 3$. The eigenfunctions are normalized by the maximum amplitude of F. The maximum amplitudes of the fluctuations are $T_{i\ max} = 8.22 \times 10^{-1}, N_{i\ max} = 3.69 \times 10^{-1}, F_{max} = 1, v_{||\ max} = 2.77 \times 10^{-1}$.

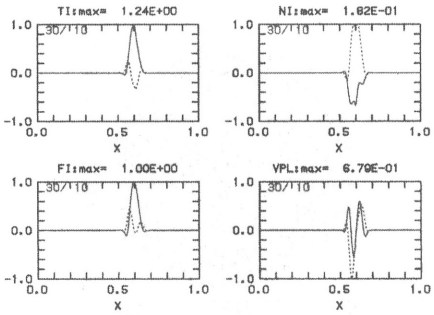

Fig. 10 Typical eigenfunctions of the slab ITG mode in the case with $q_s = 3$. The eigenfunctions are normalized by the maximum amplitude of F. The maximum amplitudes of the fluctuations are $T_{i\ max} = 1.24, N_{i\ max} = 1.82 \times 10^{-1}, F_{max} = 1, v_{||\ max} = 6.79 \times 10^{-1}$.

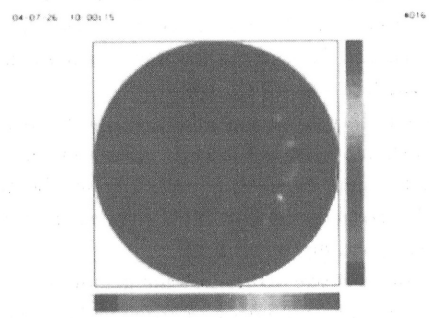

Fig. 11 The contour plot of generalized potential $F(r, \theta, \zeta = 0)$ for toroidal ITG mode. The parameters are given by $s = 1.8$, $q_s = 3$, $\eta_i = 4$, $mwd = 5$, $n = 10$ and $m = 25 \sim 35$.

outside from the original rational surface($r_s = 0.6$).

Figure 10 shows eigenfunctions of slab ITG mode $\{F, v_{||}, T_i\}$ and n_i in the case with $q_s = 3$. In this case, the mode localizes at the original rational surface, $r_s = 0.6$. The shape of eigenfunction is similar to that of toroidal mode, however, the relative amplitude of $v_{||}$ is somewhat larger than that of toroidal mode. This is because slab ITG is an unstable sound wave driven by ion temperature gradient.

Figure 11 shows the contour plot of generalized potential $F(r, \theta, \zeta = 0)$ for toroidal ITG mode. It is seen that the mode localizes at the bad curvature region and radially extends. This indicates the typical ballooning structure.

Figure 12 shows the contour plot of generalized potential $F(r, \theta, \zeta = 0)$ for slab ITG mode. In this case, the mode localizes in the radial direction and extends in the poloidal direction.

3.7 Parameter Dependence of Growth Rate

3.7.1 Toroidal Mode Number Dependence

The dependence of the growth rate on the toroidal mode number is investigated for toroidal/slab ITG mode.

Figure 13 shows the dependence of the growth rate of toroidal ITG mode on the toroidal mode number in cases with $q_s = 2$ or $q_s = 3$. Similarly, figure 14 shows the dependece of the growth rate of slab ITG mode on the toroidal mode number. The blue circle indicates the growth rate with $q_s = 2$ and red square, the one with $q_s = 3$.

Comparing these two figures, it is found that the growth rate of toroidal ITG mode is larger than that of slab ITG mode due to the toroidal coupling effect. The maximum growth rate of toroidal ITG mode with

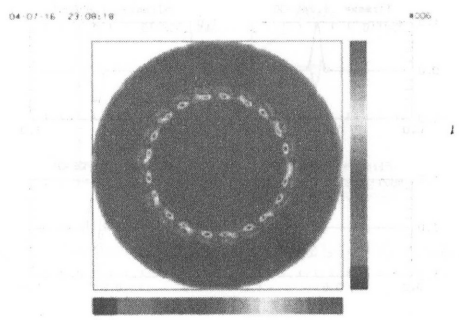

Fig. 12 The contour plot of generalized potential $F(r, \theta, \zeta = 0)$ for slab ITG mode. The parameters are given by $s = 1.8$, $q_s = 3$, $\eta_i = 4$, $n = 10$ and $m = 20$.

$q_s = 3$ is larger than that with $q_s = 2$, On the otherhand, the maximum growth rate of slab mode is almost the same in both cases. There is a similar tendency between toroidal and slab ITG modes that the miximum growth shifts to the low n side as q_s increases.

Figure 15 shows the dependence of the frequency of toroidal ITG mode on the toroidal mode number corresponding to figure 13. Also figure 16 shows the dependece of the frequency of slab ITG mode on the toroidal mode corresponding to figure 14.

It is found mode structure changes at $n = 16$ in $q_s = 3$ case. The frequency of toroidal ITG mode is linearly propotional to the toroidal mode number, on the other hand, the behavior of frequency of slab ITG mode is different from $q_s = 2$ and $q_s = 3$. It is found that eigenfunction of slab ITG mode change at $n = 16$ in the case with $q_s = 3$.

3.7.2 Shear Dependence

The dependence of the growth rate on the shear parameter is investigated for toroidal/slab ITG mode.

Figure 17 shows the dependence of the growth rate of toroidal ITG mode on the shear parameter in cases with $\eta_i = 6$ and $q_s = 2$ or 3. The blue circle corresponds to the case with $q_s = 2$ and the red square to the case with $q_s = 3$.

Figure 18 shows the dependence of the growth rate of slab ITG mode on the shear parameter. Parameters are the same as those in Figure.17. Toroidal ITG mode weakly depends on the shear parameter in both cases with $q_s = 2$ and $q_s = 3$. Slab ITG mode weakly depends on the shear parameter for $s > 2$ in both cases. In slab ITG mode, the jump of the growth rate at $s = 1.5$ for $q_s = 2$ and at $s = 1.7$ for $q_s = 3$ is observed. In order to understand and show the reason, eigenfunctions are plotted.

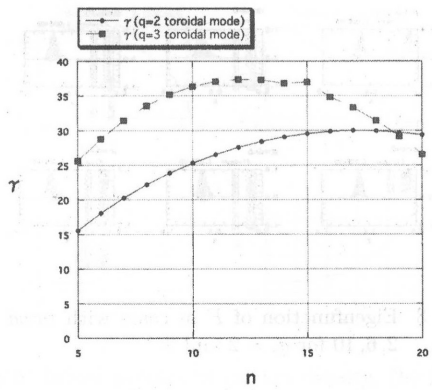

Fig. 13 The dependence of the growth rate on the mode number n of the toroidal ITG mode in cases with $q_s = 2$ or 3. The blue circle indicates the growth rate with $q_s = 2$ and red square, the one with $q_s = 3$.

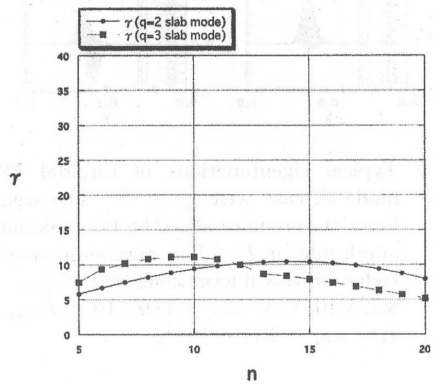

Fig. 14 The dependence of the growth rate on the mode number n of the slab ITG mode in cases with $q_s = 2$ or 3. The blue circle indicates the growth rate with $q_s = 2$ and red square, the one with $q_s = 3$.

Figure 19 shows eigenfunctions of toroidal/slab ITG mode in cases with $s = 0.8, 1.6, 2.2$ and $q_s = 3$. Similarly, figure 20 shows eigenfunctions of toroidal/slab ITG mode in cases with $s = 0.9, 1.8, 2.4$ and $q_s = 2$.

It is seen that the peak value of eigenfunction shifts inward far from $q_s = 2$ or $q_s = 3$ rational surface and indicates the different dependence of the growth rate on the shear parameter for slab ITG mode, on the other hand, in the high shear region, the peak value is located at the rational surface and indicates the weak depedence of the growth rate on the shear parameter. Unfortunately, the initial value code only gives us the largest growth rate, so that we can not follow the same branch

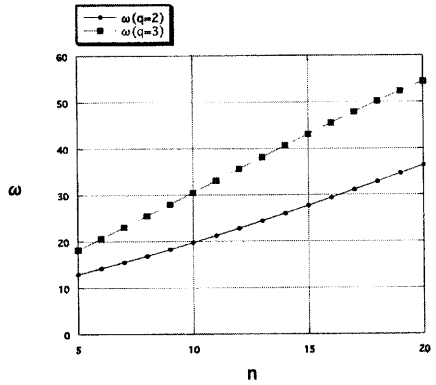

Fig. 15 The dependence of frequency of the toroidal ITG mode on toroidal mode number n, corresponding to figure 13

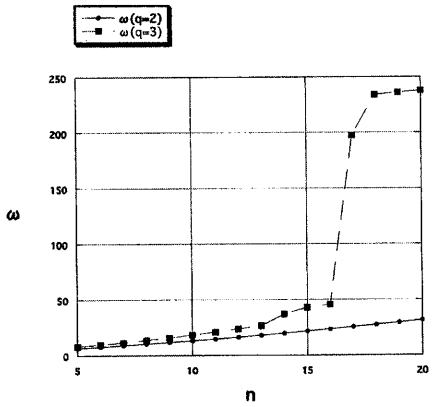

Fig. 16 The dependence of frequency of the slab ITG mode on toroidal mode number n, corresponding to figure 14

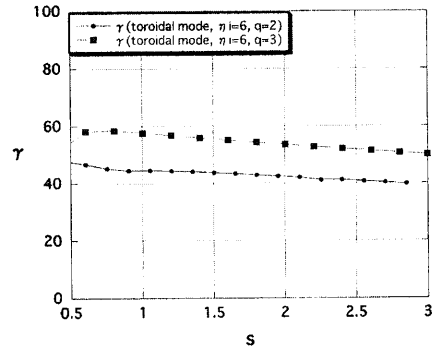

Fig. 17 The dependence of the growth rate of the toroidal ITG mode on the shear parameter in case with $\eta_i = 6$ and $q_s = 2$ or 3. The blue circle corresponds to the case with $q_s = 2$ and the red square to the one with $q_s = 3$.

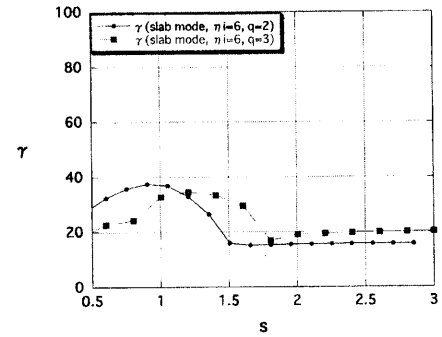

Fig. 18 The dependence of the growth rate of the slab ITG mode on the shear parameter in case with $\eta_i = 6$ and $q_s = 2$ or 3. The blue circle corresponds to the case with $q_s = 2$ and the red square to the one with $q_s = 3$.

of ITG mode in these calculations.

3.7.3 η_i dependence

The dependce of the growth rate on the η_i parameter is investigated for toroidal/slab ITG mode.

Figure 21 shows the dependence of the growth rate of toroidal ITG mode on η_i parameter in the case with $s = 1.8, q_s = 2$ or 3.

Figure 22 shows the dependence of the growth rate of slab ITG mode on η_i parameter. The parameters are the same as those in Fig 21.

The toroidal ITG mode indicates the scaling law $\gamma \propto \eta_i^{1.19}$ in the wide range of η_i parameter in the case with $s = 1.8$ and $q_s = 2$ or 3. On the other hand, the slab ITG mode indicates the different scaling law, i.e.,$\gamma \propto \eta_i^{1.24}$ for $(0 \leq \eta_i \leq 5)$ and $\gamma \propto \eta_i^{1.73}$ for $(5 \leq \eta_i \leq 10)$. The change of the scaling law corresponds to the change of the eigenfunction. For $\eta_i \leq 5$, the peak value of the eigenfunction of slab ITG mode shifts inward.

4. Nonlinear Simulation

The $\mathbf{E} \times \mathbf{B}$ nonlinearity is kept in convective term in eqs.(3.1)-(3.3).

For $m \neq 0, n \neq 0$ modes, we solve following equations; electrostatic potential:

$$\phi = \frac{\tau}{1+\tau}F - \frac{1}{1+\tau}T_i, \tag{39}$$

ion continuity equation:

$$\frac{\partial}{\partial t}\left(\frac{\tau}{1+\tau}F - \rho_*^2\nabla_\perp^2 F - \frac{1}{1+\tau}T_i\right)$$

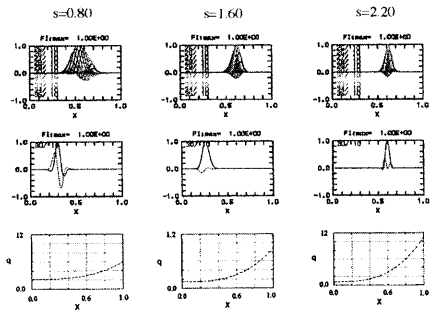

Fig. 19 The top tier shows eigenfunctions of the toroidal ITG mode and the middle tier shows eigenfunctions of slab ITG mode in the cases of $s = 0.80, 1.60, 2.20$ and $q_s = 3$. The bottom tier shows the corresponding q profiles.

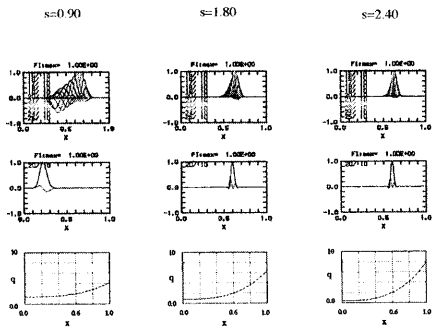

Fig. 20 The top tier shows eigenfunctions of toroidal ITG mode and the middle tier shows eigenfunctions of slab ITG mode in the cases of $s = 0.90, 1.80, 2.40$ and $q_s = 2$. The bottom tier shows the corresponding q profiles.

$$
\begin{aligned}
&= \rho_*^2[\phi, \nabla_\perp^2 F] - A v_{i||} \nabla_\| \phi \\
&-\kappa_n \frac{1}{r}\frac{\partial}{\partial\theta}(\frac{\tau}{1+\tau}F - \frac{1}{1+\tau}T_i) - A\nabla_\| v_{i||} \\
&+\epsilon_a(2\frac{1}{r}cos\theta\frac{\partial F}{\partial\theta} + 2sin\theta\frac{F}{r}) \\
&+\rho_*\frac{q}{\epsilon}\mu_i^{neo}\frac{\partial}{\partial r}(v_{i||} + \rho_*\frac{q}{\epsilon}\frac{\partial F}{\partial r}) - \rho_*^2\mu\nabla_\perp^4 F, \qquad (40)
\end{aligned}
$$

parallel momentum equation:

$$
\begin{aligned}
\frac{\partial v_{i||}}{\partial t} &= -[\phi, v_{i||}] - A\nabla_\| F + 4\mu\nabla_\perp^2 v_{i||} \\
&\quad -\mu_i^{neo}(v + \rho_*\frac{q}{\epsilon}\frac{\partial F}{\partial r}), \qquad (41)
\end{aligned}
$$

ion temperature equation:

$$
\begin{aligned}
&\frac{3}{2}\frac{\partial T_i}{\partial t} - \frac{\partial}{\partial t}(\frac{\tau}{1+\tau}F - \frac{1}{1+\tau}T_i) \\
&= -\frac{3}{2}[\phi, T_i] - \frac{3}{2}A v_{i||}\nabla_\| T_i + A v_{i||}\nabla_\|\phi
\end{aligned}
$$

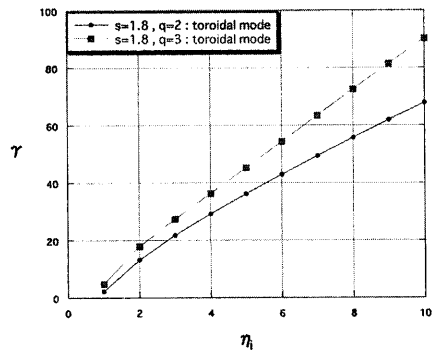

Fig. 21 The dependence of the growth rate of the toroidal ITG mode on η_i parameter in cases with $s = 1.8$ and $q_s = 2$ or 3. Blue circle indicates the growth rate with $q_s = 2$ and red square, the one with $q_s = 3$.

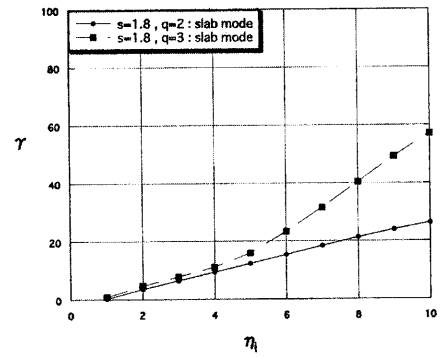

Fig. 22 The dependence of the growth rate of the slab ITG mode on η_i parameter in cases with $s = 1.8$ and $q_s = 2$ or 3. Blue circle indicates the growth rate with $q_s = 2$ and red square, the one with $q_s = 3$.

$$
\begin{aligned}
&-(\frac{3}{2}\kappa_T - \kappa_n)\frac{\tau}{1+\tau}\frac{1}{r}\frac{\partial F}{\partial\theta} + (\frac{3}{2}\kappa_T - \kappa_n)\frac{1}{1+\tau}\frac{1}{r}\frac{\partial T_i}{\partial\theta} \\
&-\frac{2}{\sqrt{\pi}}\hat{v}_{thi}A|\nabla_\||T_i + \chi_\perp\nabla_\perp^2 T_i. \qquad (42)
\end{aligned}
$$

For $m = n = 0$ mode,
electrostatic potential

$$
\phi = F - \frac{1}{1+\tau}T_i, \qquad (43)
$$

ion continuity equation:

$$
\begin{aligned}
&\frac{\partial}{\partial t}(-\rho_*^2\nabla_\perp^2 F) = \rho_*^2[\phi, \nabla_\perp^2 F] + 2\epsilon_a sin\theta\frac{\partial F}{\partial r} \\
&+\rho_*\frac{q}{\epsilon}\mu_i^{neo}\frac{\partial}{\partial r}(v_{i||} + \rho_*\frac{q}{\epsilon}\frac{\partial F}{\partial r}) - \rho_*^2\mu\nabla_\perp^4 F, \qquad (44)
\end{aligned}
$$

parallel momentum equation:

$$\frac{\partial v_{i||}}{\partial t} = -[\phi, v_{i||}] + 4\mu\nabla_\perp^2 v_{i||} - \mu_i^{neo}(v_{i||} + \rho_* \frac{q}{\epsilon}\frac{\partial F}{\partial r}), \quad (45)$$

ion temperature equation:

$$\frac{3}{2}\frac{\partial T_i}{\partial t} = -\frac{3}{2}[\phi, T_i] + \chi_\perp \nabla^2{}_\perp T_i, \quad (46)$$

where [,] is the Possison bracket defined by $[f, g] = \frac{\partial f}{\partial x}\frac{\partial g}{\partial y} - \frac{\partial f}{\partial y}\frac{\partial g}{\partial x}$.
The energy conservation relation is given by

$$\frac{dH}{dt} = -\frac{3}{2}\frac{\kappa_T}{\tau}\langle T_i \frac{1}{r}\frac{\partial \phi}{\partial \theta}\rangle - \mu_i^{neo}\langle U^2{}_p\rangle - \rho_*^2\mu\langle|\nabla_\perp^2 F|^2\rangle$$
$$-4\mu\langle|\nabla_\perp v_{i||}|^2\rangle - \frac{\chi}{\tau}\langle|\nabla_\perp T_i|^2\rangle \quad (47)$$

where

$$H = \frac{1}{2}\langle|v_{i||}|^2\rangle + \frac{1}{2}\rho_*^2\langle|\nabla_\perp F|^2\rangle$$
$$+\frac{1}{2}\frac{1+\tau}{\tau}\langle|\phi|^2\rangle + \frac{1}{2}\frac{3}{2}\langle\frac{T^2{}_i}{\tau}\rangle. \quad (48)$$

The heat flux is calculated by

$$q = \langle\tilde{T}\tilde{v}_{E\times B}\rangle$$
$$= \sum_{m,n}\tilde{T}^*_{m,n}(-ik_y\phi_{m,n}) = -\chi\frac{(\tilde{T}_{0,0} + T_{0,0})}{dr}, \quad (49)$$

where $\tilde{T}^*_{m,n} = \tilde{T}_{-m,-n}$ is the complex conjugate of $\tilde{T}_{m,n}$.

In the nonlinear simulations, with parameter of $mwd = 5$, $s = 1.1$ and $\eta_i = 4$, fluctuating energy is caluculated and structural formation such as zonal flow is investigated. The nonlinear calculation uses finite-difference in r, Fourier expansion in (θ, ψ) and predictor-corrector time.

4.1 Fourier Modes and Disposal Mode

Fourier spectrum used in nonlinear simulations is shown in figure 23. The maximum mode number used in these simulations is $M = 165, N = 80$, respectivly. The blue lines indicate modes which are disposed at each time step . This is because the reflection of spectrum in Fourier space is to avoid for energy saturation. In these simulations, we don't solve $\tilde{T}_{0,0}$ i.e., $\tilde{T}_{0,0} = 0$

4.2 Zonal Flow Formation and Transport

Figure 24 shows the time evolution of fluctuating energy in case with $\mu_i^{neo} = 1$. The saturation is attained at $t \geq 0.8$. Figure 25 shows the contour plots of generalized potential at $t = 0.2$ and $t = 1.0$. In the linear phase $t = 0.2$, linear eigenfunction of toroidal ITG mode is clearly seen and in the nonlinear phase $t = 1.0$, the zonal flow is formed. The finite structures which comes from $m \simeq 10$ contribution is also observed. Figure 26 shows power spectrum of fluctuating electrostatic energy at $t = 0.2$ and $t = 1.0$. It is seen that in the linear

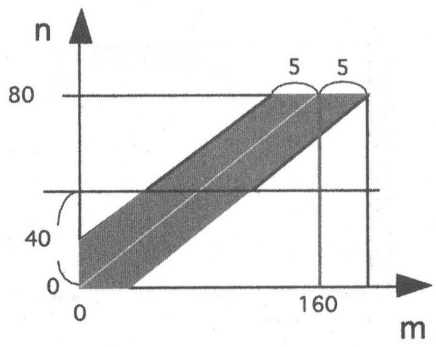

Fig. 23 Fourier spectrum used in the nonlinear simulation. The blue lines indicates modes which are disposed at each time step.

phase, high n modes have some contents of energy. This is due to the noise given at the initial condition. There is the peak around $m \cong 20$, this corresponds to the ITG mode. In the nonlinear phase, cascade and inverse cascade occur and steady state spectrum is obtained. It should be noticed that the circles with amplitude 10^{-15} corresponds to the disposal modes, it's real value is zero in simulations, however, to show them we set its value 10^{-15} in the semi-log graph.

4.3 Neoclassical Effect on Transport of χ_i in Cases with/without $\mu_i{}^{neo}$

In this section, we compare thermal diffusivity χ_i in cases with $\mu_i{}^{neo} = 1$ and $\mu_i{}^{neo} = 0$. Figure 27 shows the radial profile of thermal diffusivity. The peak of χ_i is located in the original rational surface($r_s = 0.6$) in linear phase, however, the peak spreads over the rational surface according to the increase of the time. This broad enhancement of χ_i might correspond to transport enhancement by nonlinear coupled modes. The double peak of χ_i is formed by transport suppression by zonal flow. In the nonlinear phase $t = 1.0$, χ_i with neoclassical viscosity is somewhat larger than without it inside the original rational surface $r_s \leq 0.6$. This might correspond to the lack of stabilization for drift wave turbulence due to the flow shear. On the other hand, the opposite tendency is observed outside the rational surface. Figure 3.24 shows the time evolution of zonal flow energy. The weak damping of zonal flow is seen at $t \geq 0.8$. The simulation is global not local so that the local theory may not simply apply for our case. In any case, systematic parameter survey is necessary to clearify neoclassical damping effect on the saturation level. It is left for future work.

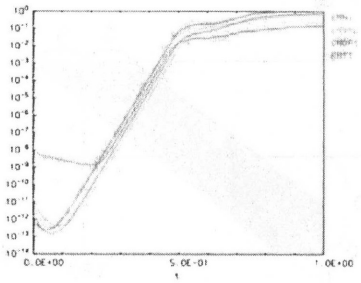

Fig. 24 The time evolution of the fluctuating energy in cases with $\mu_i^{neo} = 1$. The saturation is attained at $t \geq 0.8$.

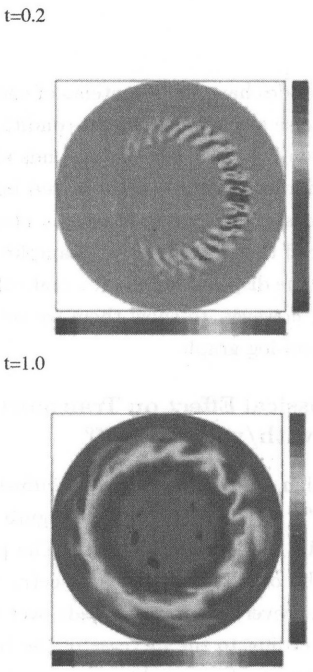

Fig. 25 The contour plots of generalized potential at $t = 0.2$(linear phase) and $t = 1.0$(nonlinear phase).

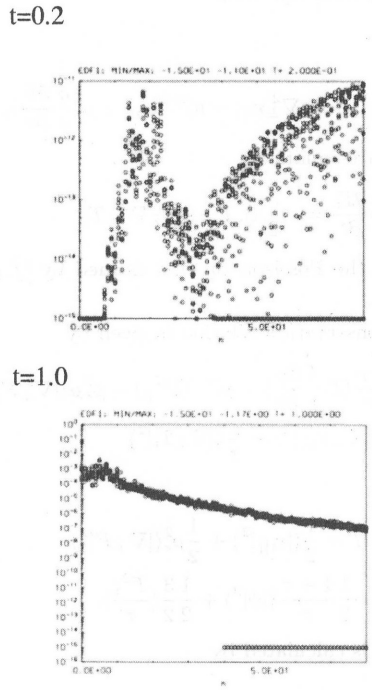

Fig. 26 Power spectrum of fluctuating electrostastic energy at $t = 0.2$ and $t = 1.0$.

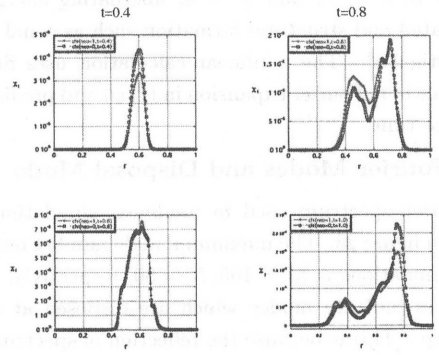

Fig. 27 The radial profile of the ion thermal diffusivity χ_i at $t = 0.4, 0.6, 0.8$ and 1.0. The red circle corresponds to the case with the neoclassical viscosity and the blue square to the one without the neoclassical viscosity.

5. Summary

The linear stability of toroidal and slab ITG mode is investigated based on three-field reduced MHD equation in which ion neoclassical viscosity and fluctuating ion parallel flow are taken into account.

It is found that (1) the growth rate of the toroidal mode is larger than that of the slab mode due to toroidal coupling, (2) the growth rate of toroidal and slab ITG mode weakly depends on shear parameter, (3) the growth rate scales as $\gamma \propto {\eta_i}^{1.2}$ for toroidal mode and $\gamma \propto {\eta_i}^{1.7}$ for slab mode. In the weak shear limit, the peak of the eigenfunction shift inward for the original rational surface and different parameter dependence of the growth rate is observed.

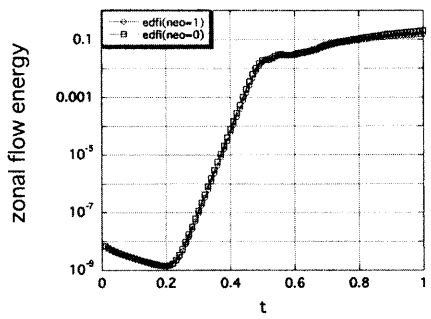

Fig. 28 The time evolution of zonal flow energy in cases with $\mu_i^{neo} = 1$ or $\mu_i^{neo} = 0$. The circle corresponds to the cases with $\mu_i^{neo} = 1$ and square, the case with $\mu_i^{neo} = 0$.

Next, the nonlinear simulations are performed to investigate the flow effect on the saturation level. It is found that (1) zonal flow is formed in the saturation phase similar to the result by flux tube simulation, however, it is accompanied with structure with $m \cong 10$, (2) the neoclassical viscosity weakly affects the flow damping, therefore, the saturation level of drift wave turbulence, (3) χ_i with neoclassical viscosity is larger than that without it inside the original rational surface $r_s = 0.6$. On the other hand, opposite tendency is observed outside the rational surface.

The systematic parameter survey is necessary to clearify neoclassical damping effect on the saturation level of ITG turbulence in global simulation. It is left for future work.

Acknowledgment

The author would like to thank all of those who have contributed to the completion of this thesis. He is greatly indebted to Professor S. -I. Itoh continual guidance and Dr. M. Yagi for useful comments. Special thanks to Dr. M. Azumi (Japan Atomic Energy Research Institute), Dr. F. Spineanu, Dr. M. Vlad and Dr. P. Diamond for fruitfull discussions and comments. He also would like to thanks my colleague; Miss. E. Mori and Miss. A. Tsukamoto.

This work is partly supported by the collaboration program of Research Institute for Applied Mechanics, Kyushu University and the Grant-in-Aid for Scientific Research of MEXT of Japan.

Finally, the author wishes to thank his family for their supports.

References

1) R. Z. Sagdeev, V. D. Shapiro, and V. I. Shevchenko, Sov. J. Plasma Phys. 4 (1978) 306.
2) W. Horton, Rev. Mod. Phys 71 (1999) 735 .
3) J. Y. Kim, W. Horton, D. I. Choi, S. Migliuolo and B. Coppi, Phys. Fluids B4 (1992) 152.
4) Z. Lin, S. Ethier, T. S. Hahm, and W. M. Tang Phys. Rev. Lett. 88 (2002) 195004.
5) M. Ottaviani and G. Manfredi, Phys. Plasmas 6 (1999) 3267.
6) A. Hirose, Phys. Rev. Lett 55 (1985) 504.
7) M. A. Beer and G. W. Hammett Phys. Plasmas 3 (1996) 4046.
8) J. Anderson, H. Nordman, R. Singh, and J. Weiland Phys. Plasmas 9 (2002) 4500.
9) A. I. Smolyakov, P. H. Diamond, and V. I. Shevchenko Phys. Plasmas 7 (2000) 1349.
10) M. Yagi, J. P. Wang, Y. B. Kim, and M. Azumi Phys. Fluids B5 (1993) 1179.
11) K. Mima and A. Hasegawa Phys. Fludis 21 (1978) 81.
12) Z. Gao, J. Q. Dong, and H. Sanuki Phys. Plasmas 11 (2004) 3053.
13) J. Li and Y. Kishimoto Phys. Rev. Lett 89 (2002) 1150002-1.
14) Z. Gao, H. Sanuki, K. Itoh, and J. Q. Dong Phys. Plasmas 10 (2003) 2831.
15) J. T. Mendonca, R. Bingham, and P. K. Shukla Phys. Rev. Lett 68 (2003) 016406-1.
16) F. Romanelli and F. Zonca Phys. Fludis B 5 (1993) 4081.
17) Introduction to Plasma Physics, Robert J Goldston and Paul H Rutherford, IOP Publishing Ltd, 1995.
18) A. Hasegawa, and M. Wakatani, Phys, Rev. Lett 59 (1987) 1581.
19) Tokamaks Second Edition, John Wesson, Oxford Science Publications CLARENDON PRESS-OXFORD, 1997.
20) J. W. Connor, R. J. Hastie, and J. B. Taylor, Phys, Rev. Lett 40 (1978) 396.
21) Z. LIn, T. S. Hahm, W. W. Lee, W. M. Tang, Phys. Rev. Lett 83 (1999) 3645.
22) M. N. Rosenbluth, F. L. Hinton, Phys. Rev. Lett 80 (1998) 724.
23) K. Itoh, K. Hallatschek, plasma Phys. Control. Fusion 46 (2004) 335.
24) M. N. Rosenbluth, F. L. Hinton, M. N. Rosenbluth, plasma Phys. Control. Fusion 41 (1999) 653.